Technical note: High-resolution analyses of concentrations and sizes of refractory black carbon particles deposited on northwest Greenland over the past 350 years – Part 1. Continuous flow analysis of the SIGMA-D ice core using a Wide-Range Single-Particle Soot Photometer and a high-efficiency nebulizer

Kumiko Goto-Azuma[1,2], Remi Dallmayr[1,a], Yoshimi Ogawa-Tsukagawa[1], Nobuhiro Moteki[3], Tatsuhiro Mori[4], Sho Ohata[5], Yutaka Kondo[1], Makoto Koike[6], Motohiro Hirabayashi[1], Jun Ogata[1], Kyotaro Kitamura[1], Kenji Kawamura[1,2], Koji Fujita[5], Sumito Matoba[7], Naoko Nagatsuka[1,c], Akane Tsushima[1,b], Kaori Fukuda[1], and Teruo Aoki[1]

[1]National Institute of Polar Research, Tachikawa, Tokyo, 190-8518, Japan
[2]SOKENDAI, Shonan Village, Hayama, Kanagawa, 240-0193, Japan
[3]Tokyo Metropolitan University, Hachioji, Tokyo, 192-0397, Japan
[4]Keio University, Yokohama, Kanagawa, 223-8521, Japan
[5]Nagoya University, Nagoya, 464-8601, Japan
[6]University of Tokyo, Bunkyo-ku, 113-0033, Japan
[7]Hokkaido University, Sapporo, 060-0819, Japan
[a]Now at Alfred Wegener Institute for Polar and Marine Research, Bremerhaven, Germany
[b]Now at Meteorological Research Institute, Tsukuba, Ibaraki, 305-0052, Japan
[c]Now at Japan Agency for Marine-Earth Science and Technology, Yokosuka, Kanagawa, 237-0061, Japan

Correspondence to: Kumiko Goto-Azuma (kumiko@nipr.ac.jp)

Abstract. Ice cores can provide long-term records of refractory black carbon (rBC), an important aerosol species closely linked to the climate and environment. However, previous studies of ice cores only analysed rBC particles with diameter of <~~600~~500–~~850~~ nm, which could have led to underestimation of rBC mass concentrations. Information on the size distribution of rBC particles is very limited, and there are no Arctic ice core records of the temporal variation in rBC size distribution. In this study, we applied a recently developed improved technique to analyse the rBC concentration in an ice core drilled at the SIGMA-D site in northwest Greenland. The improved technique, which uses a modified Single-Particle Soot Photometer and a high-efficiency nebulizer, widens the measurable range of rBC particle size. For high-resolution continuous analyses of ice cores, we developed a continuous flow analysis (CFA) system ~~(resolution: 10–40 mm)~~. Coupling of the improved rBC measurement technique with the CFA system allows accurate high-resolution measurements of the size distribution and concentration of rBC particles with diameter between 70 nm and 4 μm, with minimal particle losses. Using this technique, we reconstructed

the size distributions and the number and mass concentrations of rBC particles during the past 350 years. On the basis of the size distributions, we assessed the underestimation of rBC mass concentrations measured using the conventional ~~method~~SP2s. For the period 2003–2013, the underestimation of the average mass concentration would have been 12%–~~17~~31% for the SIGMA-D core.

1 Introduction

Black carbon (BC), which is emitted from both anthropogenic and natural sources (e.g., fossil fuel combustion and biomass burning), can affect Earth's radiation budget by absorbing sunlight and reducing the albedo of snow and ice surfaces (e.g., Bond et al., 2013; Mori et al., 2019; Matsui et al., 2022; Moteki, 2023 and references therein). Particles of BC can also affect cloud microphysical processes by acting as cloud condensation nuclei (CCN) or ice nucleating particles (e.g., Bond et al., 2013; AMAP, 2021), thereby indirectly affecting the radiation budget. Over the past half-century, the Arctic has warmed at a rate four times faster than that of the global average (Rantanen et al., 2022), leading to drastic changes such as sea ice retreat, enhanced losses of glacier mass, and ecosystem changes. It is therefore important to evaluate the effects of BC on the radiation budget in the Arctic. Freshly emitted BC particles are initially hydrophobic, but gradually become coated with other aerosol species, transforming into internally mixed hydrophilic particles during transport (*e.g.* Mori et al., 2017; Matsui, 2017; Matsui and Mahowald, 2017). These hydrophilic BC particles can be activated as CCN, depending on their size and mixing state, and are eventually deposited on the earth's surface via precipitation. The size distribution of BC particles influences not only their ability to act as CCN but also their transport and deposition processes, thereby controlling the temporal and spatial variability of BC concentrations. In addition, size distribution affects the light absorption properties of BC particles. Therefore, the size distribution as well as concentrations of BC particles is a key parameter for understanding the impacts of BC on Earth's radiation budget. ~~Furthermore, BC emitted from fossil fuel combustion and large forest fires can affect air quality, ecosystems, and human health (Keane et al., 2008; Wang et al., 2021). Climate change can alter the frequency and magnitude of biomass burning events and hence influence BC emissions. In recent decades, global warming appears to have promoted increased occurrence of huge forest fires, which have triggered serious damage to forests, agriculture, and social infrastructure and sometimes even caused human casualties (Brown et al., 2023; Keeley and Syphard, 2021). Consequently accurate projections of the frequency and magnitude of future huge biomass burning events urgently need to be conducted to minimize the related potential hazard. To understand the effects of BC on the radiation budget and of the impacts of climate change on BC emissions,~~

~~d~~Data acquired since the pre-industrial period are particularly valuable because we cannot fully understand the anthropogenic effects without characterizing BC in a pristine environment. ~~Size distribution and concentration are important parameters that affect the radiative properties of BC particles.~~ However, no direct measurements of the size distributions and concentrations of BC particles were performed prior to the past few decades despite numerous studies based on observations and aerosol/climate models (e.g., Bond et al., 2013 and references therein).

Ice cores can provide long-term records of BC deposition. Following development of the Single-Particle Soot Photometer (SP2; Droplet Measurement Technologies, USA) (Stephens et al., 2003; Baumgardner et al., 2004), it has been possible to measure refractory black carbon (rBC), the terminology used for incandesce-based BC measurements (Petzold et al., 2013; Lim et al., 2014), even in Arctic and Antarctic ice cores that contain very low concentrations of rBC particles (McConnell et al., 2007; Zdanowicz et al., 2018; Osmont et al., 2018; Zennaro et al., 2014; Bisiaux et al., 2012a, b; Arienzo et al., 2019) ~~have become possible~~. Moreover, attachment of a coupled SP2 and nebuli~~z~~ser system to a continuous flow analysis (CFA) system allowed continuous and high temporal-resolution analyses of rBC in ice cores drilled at a site with little summer melting (McConnell et al., 2007; Lim et al., 2017; Bisiaux et al., 2012a, 2012b; Arienzo et al., 2017). Many previous SP2 analyses of rBC in ice cores, regardless of whether they used a CFA system, adopted the U5000AT ultrasonic nebuli~~z~~ser (Teledyne CETAC, USA) system (or a similar ultrasonic nebuli~~z~~ser) to aerosolize rBC particles in melted ice core samples before their introduction to the SP2 (McConnell et al., 2007; Zennaro et al., 2014; Zdanowicz et al., 2018; Du et al., 2020; Kaspari et al., 2011; Wang et al., 2015; Bisiaux et al., 2012a, 2012b; ;rienzo et al., 2017). Owing to the complex and temporally variable size dependence of the extraction efficiency of ~~an~~ the U5000AT ultrasonic nebuli~~z~~ser system (Schwarz et al., 2012; Wendl et al., 2014; Ohata et al., 2013; Mori et al., 2016), large uncertainties are associated with the derived size distributions and concentrations. Obtaining accurate estimation of the size distribution of rBC particles on a routine basis is not easy using the U5000AT nebulizer system. While Kaspari et al. (2011) reported mass size distributions of rBC in two samples from a Mt. Everest ice core using the U5000AT nebulizer system, ~~L~~long-term ice core records of the size distribution of rBC particles obtained using this type of nebulizer system have not been reported. On the contrary, ~~for BC particles with diameter of 100-1000 nm, a report indicates~~ Wendl et al. (2014) demonstrated size-independent extraction efficiency (<15% variability) ~~for~~ of the APEX Q jet nebulizer system (High-Sensitivity Sample Introduction System, Elemental Scientific Inc., USA) for rBC particles in the 100-1000 nm diameter rage ~~(Wendl et al., 2014)~~. Lim et al. (2014) also reported size-independent extraction efficiency (<10% variability) of the APEX Q nebulizer system for rBC particles with diameters between 60 and 500 nm. As a

result, recently, the APEX-Q nebulizer system is becoming the standard within the ice core community. Using an APEX Q nebulizer system and an SP2 attached to a CFA system, Lim et al. (2017) analysed ice cores from Mt. Elbrus (western Caucasus Mountains) and reported temporal variability in the size and concentration of rBC particles with diameters between 70 and 620 nm during 1825–2013. However, to date, no BC size distribution data from Arctic ice cores have been published.

Snow and hence ice cores could contain much larger BC particles than those typically observed in the atmosphere (Schwarz et al., 2012, 2015). The particle size range typically measurable by an off-the-shelf SP2 ~~(hereafter, the standard SP2)~~ is from approximately 70 to ~~850–9~~400-500 nm (Moteki and Kondo, 2010; Kaspari et al., 2011~~Ohata et al., 2011; Mori et al., 2016~~), i.e., particles with diameter of >~~850–95~~00 nm cannot be detected using ~~the~~ an ~~standard~~ off-the-shelf SP2. Moteki and Kondo (2010) extended the upper limit of measurable rBC particle diameters to 850-900 nm (Moteki and Kondo, 2010; Ohata et al., 2011). More recently, an off-the-shelf instrument called the Single Particle Soot Photometer Extended Range (SP2-XR; Droplet Measurement Technologies, USA), with measurable diameter range 50-800 nm, has become available. However, to our knowledge, no ice core rBC data produced by the SP2-XR have been published.

The extraction efficiency of the U5000AT ultrasonic nebulizer system at a flow rate of 0.19 mL min^{-1} ~~is~~ has been reported to be 10%–12% for the particle diameter range of approximately 200–500 nm; it decreases sharply for diameters >500 nm and decreases to approximately 2% for particles with diameter of 700 nm (Ohata et al., 2013; Mori et al., 2016). It also decreases for diameters < 200 nm (Ohata et al., 2013; Wendl et al., 2014; Mori et al., 2016). Thus, unless the size dependent extraction efficiency is carefully measured, as done by Moteki and Kondo (2010) and Ohata et al. (2011), measurements obtained using this nebulizer system could have large uncertainties not only in size distribution but also in mass concentration if the ice core samples contain BC particles with diameter of >500 nm, even if an SP2 with extended upper limit is used.

Modern snow and ice core samples from the Arctic, including Greenland, do contain substantial fractions of rBC particles with diameter of >~~600–~~500 nm (Mori et al., 2019). Similarly, modern snow from Antarctica also contains a consicerable proportion of rBC particles with diameters >500 nm (Kinase et al., 2020). If mass size distributions follow lognormal size distributions with mass median diameters <500 nm, mass concentrations for diameters > 500 nm can be estimated using lognormal fitting. However, non-lognormal mass size distributions with substantial concentrations of particles with diameters >850-900 nm have been reported for Arctic snow (Mori et al., 2019). Non-lognormal mass size distributions have also been observed in a Mt. Everest ice core, which contained substantial mass concentrations of rBC particles larger than the upper measurable diameter limit of 500 nm (Kaspari et al., 2011). Furthermore, bimodal mass size distributions with

secondary modes diameters >500 nm have been reported for Antarctic snow (Kinase et al., 2020). Therefore, it is important to extend the measurable diameter range of rBC particles beyond 900 nm and to employ a nebulizer system with a high and size-independent extraction efficiency.

Mori et al. (2016) developed an improved technique for accurate measurement of the size distributions and concentrations of rBC particles with diameter between 70 nm and 4 μm in water samples. They used a Wide-Range SP2 (i.e., an SP2 modified to widen the measurable size range of rBC particles) and a Marin-5 high-efficiency concentric pneumatic nebulizer system (Teledyne CETAC, USA). For accurate, continuous, and high-resolution analyses of the concentrations and size distributions of rBC particles in polar ice cores, we combined the improved rBC measurement technique and a CFA system developed at the National Institute of Polar Research (NIPR). We used this system to analyse an ice core drilled at SIGMA-D in northwest Greenland (Matoba et al., 2015; Nagatsuka et al., 2021), following which we reconstructed the concentrations and size distributions of rBC particles with diameter between 70 nm and 4 μm for the past 350 years. In this paper (called Part 1), we describe the coupled CFA-rBC measurement system and evaluate its performance. We compare the nebulizer efficiencies of Marin-5, APEX-Q, and U5000AT nebulizer systems; assess the stability of the efficiency of Marin-5 nebulizer system; examine the dispersion of the CFA-rBC signal; provide the evidence of minimal losses of rBC particles within the CFA-rBC system; and show examples of rBC size distributions. ~~And~~ Since it is important to compare the data that our new rBC measurement system produced and the valuable data from the previous ice core rBC measurements, we also estimated the extent of underestimations in mass concentrations measured with the off-the-shelf SP2s. ~~the data that it produced.~~ Using the new continuous high-resolution data, we investigated the seasonal variations in concentrations and size distributions of rBC particles originating from both anthropogenic and biomass burning emissions and their temporal changes. In a companion paper (Part 2), we discuss the derived results in detail.

2 Methods

2.1 Continuous flow analysis (CFA) system

To undertake high-resolution continuous analyses of ice cores, we developed a CFA system at NIPR. Figure 1 shows a schematic of the NIPR CFA system used to analyse the SIGMA-D core. It consists of a melting unit, debubbler unit, inductively coupled plasma–mass spectrometer (ICP-MS) unit, stable water isotope unit, microparticle unit, methane unit,

and fraction collector unit in addition to an rBC unit. The rBC unit, ICP-MS unit, microparticle unit, and methane unit were added to an earlier version of the NIPR CFA system described by Dallmayr et al. (2016). The melting unit, debubbler unit, and the stable water isotope unit were the same as those used in the earlier version. Details of the melting unit, the ICP-MS unit, and the stable water isotope unit are provided in Appendix A. Although

~~An ice core sample (cross section: 34 mm × 34 mm, length: ~0.5 m) was placed on a melt head inside a freezer. An 850 g weight was placed on top of the ice sample to allow stable melting. Before the ice core sample was completely melted, another similarly sized ice core sample was stacked on top of the first sample to maintain continuous melting of the ice samples. To promote melting, heaters are inserted into the melt head (Bigler et al., 2011; Osterberg et al., 2006). In the earlier NIPR CFA system, we used a melt head developed at the University of Maine (Osterberg et al., 2006). However, in this study, we used a melt head similar to the one used by Bigler et al. (2011) for the depth interval between 11.3 and 112.8 m of the SIGMA-D core. The University of Maine type melt head, designed principally for use in firn core analyses, is not airtight. For methane analysis, we had to use an airtight melt head such as the one used by Bigler et al. (2011). For the depth interval between 6.1 and 11.3 m of the SIGMA-D core, we used the University of Maine type melt head (Dallmayr et al., 2016; Osterberg et al., 2006) to reduce water percolation through the porous firn caused by capillary action (Osterberg et al., 2006). For depths < 49.3 m, methane measurement was not performed.~~

~~The depth of an ice core sample is assigned using a laser positioning sensor (LKG-G505, Keyence, Japan), which determines the distance from the sensor to the top of the weight (Dallmayr et al., 2016). A typical melt speed, regulated by the voltage applied to the heaters in the melt head, is 30 mm min^{-1}. The depth resolution with this melt speed is approximately 0.3 ± 0.1 mm. The meltwater collected in the contamination free inner part of the melt head is drawn through perfluoroalkoxy alkane tubing, an injection valve, and the debubbler unit by a peristaltic pump (Minipuls3 MP-2, Gilson, USA). Following removal of air bubbles by the debubbler unit, the meltwater is introduced to the different measurement units and to the fraction collector unit using peristaltic pumps (Reglo Digital ISM596, ISMATEC, Germany). Before each unit, an electrical conductivity cell (conductivity meter Model 1056, Amber Science Inc., USA) is placed as close as possible to the unit to synchronise the depths of the ice core data acquired by the different measurement units and the depths of the meltwater samples collected by the fraction collector unit (McConnell et al., 2002; Dallmayr et al., 2016). A length of approximately 7 m of the ice core was melted once or twice a week.~~

~~The ICP-MS unit consists of an ICP-MS (7700 ICP-MS, Agilent Technologies, USA). The elements ^{23}Na, ^{24}Mg, ^{27}Al, ^{39}K, ^{43}Ca, and ^{56}Fe were each measured at a 3.00 s interval. Additionally, ^{89}Y was measured at a 3.00 s interval to check the stability of the ICP-MS. Data acquisition times for ^{23}Na, ^{24}Mg, ^{27}Al, ^{39}K, ^{43}Ca, ^{56}Fe, and ^{89}Y were 0.02, 0,1, 0.2, 0.1, 2.27, 0.252, and 0.044 s, respectively. In this study, we used mainly ^{23}Na data to date the core. The concentration of each of the elements was calibrated both before and after the CFA measurements of the day using a multi-element standard solution (XSTC-331, Spex CertiPrep, USA) diluted with ultra-pure water (Milli-Q water, Milli-Q Advantage, Merck Millipore, Germany). The detection limit, defined as [3σ of the blank value + the intercept of the calibration line], of ^{23}Na is 0.5 μg L^{-1}.~~

~~The stable water isotope unit is same as that used by Dallmayr et al. (2016). It consists of a vaporization module (Gkinis et al., 2011; Dallmayr et al., 2016) and a wavelength-scanned cavity ring-down spectrometer (L2130-i, Picarro Inc., USA). We calibrated the spectrometer by analysing three sets of laboratory water isotope standards after the CFA measurements of the day (Dallmayr et al., 2016). These laboratory standards were calibrated with VSMOW2 and SLAP2 standards purchased from the International Atomic Energy Agency. Details of calibrations and the performance of the stable water isotope unit have been described in a previous study (Dallmayr et al., 2016).~~

~~T~~the NIPR CFA system includes a microparticle unit, methane unit, and fraction collector unit consisting of three fraction collectors~~. However~~, we do not discuss them further here because the data that they provided are not relevant. The specification and performance of each of these units will be reported elsewhere.

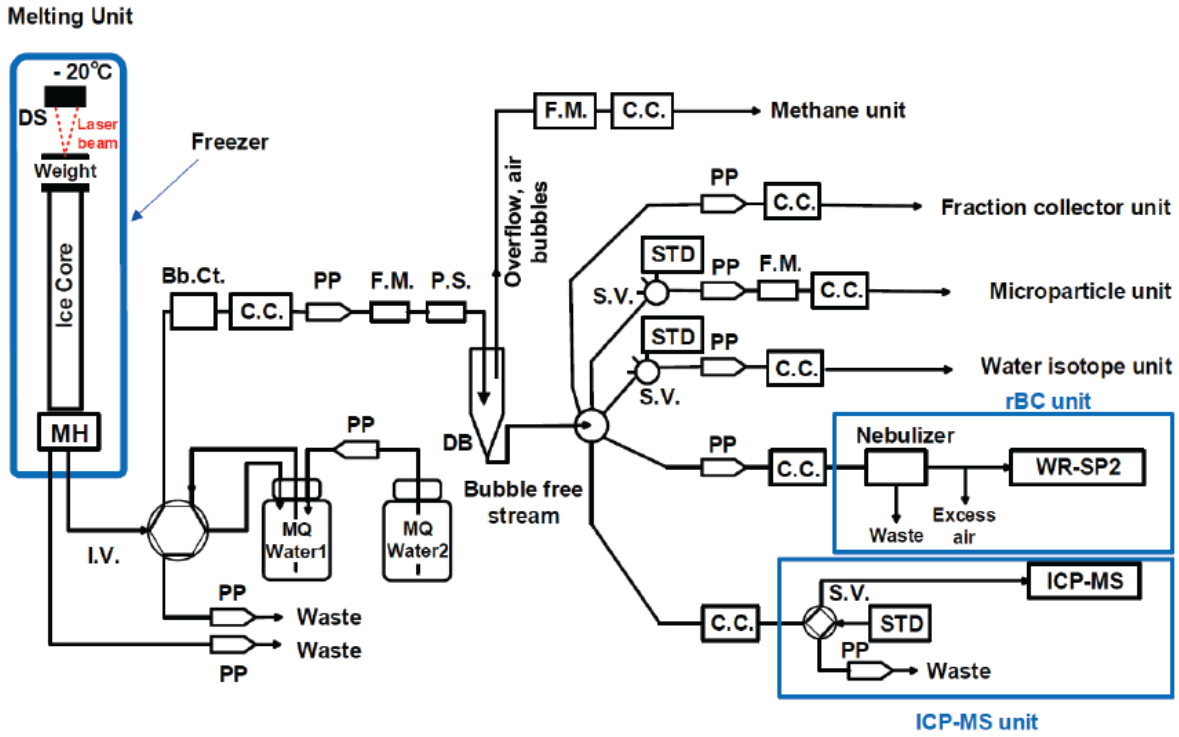

Figure 1: Schematic of the CFA system developed in this study.

DS: displacement sensor, MH: melt head, I.V.: injection valve, S.V.: selection valve, Bb.Ct.: bubble counter, C.C.: conductivity cell, PP: peristaltic pump, F.M.: flow meter, P.S. pressure sensor, DB: debubbler, STD: standard, MQ Water: ultra-pure water generated by a Milli-Q system.

2.2 Refractory ~~B~~black carbon (rBC) unit

We applied the improved technique developed by Mori et al. (2016) to the rBC unit of the NIPR CFA system. The rBC unit consists of a Wide-Range SP2 (Mori et al., 2016) and a concentric pneumatic nebulizer system (Marin-5, Teledyne CETAC, USA). The SP2 detects the incandescence signal from individual rBC particles induced by irradiation of an Nd-YAG laser (Stephens et al., 2003; Baumgardner, 2004; Schwarz et al., 2006). The ~~standard~~ off-the-shelf SP2 can detect rBC particles with diameter of between 70 and ~~850~~400 ~~95~~00 nm, assuming rBC particle density of 1.8 g cm^{-3} (Moteki and Kondo, 2010; Kaspari et al., 2011). The SP2 modified by Moteki and Kondo (2010) can meausure rBC particles with diameters between approximately 70 and 850-900 nm, whereas the off-the-shelf SP2-XR can measure rBC particles with diameters between approximately 50 and 800 nm. For the Wide-Range SP2, Mori et al. (2016) expanded the upper limit of the measurable

diameter to 4 μm by modifying the detection unit of the standard SP2. ~~Hence~~As a result, the Wide-Range SP2 can detect rBC particles with diameters of between approximately 70 nm and 4 μm. We used the "Standard SP2 Software" and the "Probe Analysis Package for Igor (PAPI)", both provided by DMT, to acquire and process the incandescent signal in binary data and convert it to text format. Then we used our original code to calculate the mass and size of BC particles.

The meltwater that passes through the debubbler unit is fed to the Marin-5 nebulizer system at a constant flow rate of 6.3 μL s^{-1} by a peristaltic pump (REGLO Digital ISM596, ISMATEC, Germany) running at 7.50 rpm. We measured the flow rate before and after each CFA session. As the flow rate slightly (~5%) decreased after each CFA session, likely due to tube wear, we adjusted the flow rate of the peristaltic pump before the next CFA session. This approach allowed us to maintain a nearly constant flow rate with less than 5% variability. Under these conditions, no pulsed flow was observed. The Marin-5 nebulizer system was equipped with a MicroMist U-Series nebulizer AR30-1-UM05E (Glass Expansion, Australia). We used G3 Grade air as a carrier gas for the nebulizer. The flow rate of the carrier gas ~~is~~ was 15.2 cm^3 s^{-1} at standard temperature and pressure (i.e., 0 °C and 1013 hPa, respectively). The nebulizer system converts a fraction of the meltwater into water droplets that are immediately heated to 140 °C in a spray chamber, generating a mixture of rBC particles, non-rBC particles, and water vapor. After the non-aerosolized meltwater is removed via the drains, this mixture is cooled to 3 °C in a condenser, thereby removing the water vapor. Hence, only rBC and non-rBC particles are introduced to the Wide-Range SP2 at a flow rate of 12 cm^3 min^{-1}. The details of the Wide-Range SP2 and the Marin-5, together with assessment of their performance, have been reported by Mori et al. (2016).

To derive the relationship between the peak incandescence signal and the mass of each rBC particle (Stephens et al., 2003; Schwarz et al., 2006), we used fullerene soot (Alpha Aesar Inc., USA, Lot No. 20W054) as a standard material (Moteki and Kondo, 2010). We used an Aerosol Particle Mass Analyzer (Moteki and Kondo, 2010) Model 3601 (APM-II, KANOMAX, Japan) to extract fullerene soot particles with a mass range of 1.19–203 fg, corresponding to mass equivalent diameters of 100–600 nm. Following Mori et al. (2016), we produced two calibration curves for rBC masses below and above 10 fg, which corresponds to the mass equivalent diameter of 220 nm. Mass equivalent diameters of rBC particles were calculated assuming an rBC particle density of 1.8 g cm^{-3} (Moteki and Kondo, 2010).

For accurate measurement of rBC particle size, the nebulizer efficiency and its size dependence must be known (Ohata et al., 2013; Mori et al., 2016). However, to the best of our knowledge, previous ice core studies using an SP2 rarely used ~~considered~~ nebulizer efficiency determined by measurements, except those conducted by Wendl et al. (2014), Lim et al. (2014)

and Lim et al. (2017). We determined nebulizer efficiency using Polystyrene Latex Sphere (PSL) suspensions with known number concentrations (Ohata et al., 2011, 2013; Mori et al., 2016) for diameters of >200 nm. We used PSL particles supplied by two manufacturers. The diameters of the PSL particles supplied by Polysciences Inc., USA (NIST Traceable Particle Size Standard), were 207, 288, 505, 603, 707, 814, 1025, and 1537 nm, and the diameters of those supplied by Thermo Fisher Scientific Inc., USA, were 2000 and 3000 nm. For diameters of <200 nm, we used AquaBlack 162 (AB-162, Tokai Carbon Co. Ltd., Japan), which is a laboratory standard for rBC particles suspended in water (Mori et al., 2016; Ohata et al., 2011; Ohata et al., 2013). The number concentration of the PSL particles and that of the AquaBlack samples in the carrier gas were measured by the Wide-Range SP2, and compared with those of the PSL suspensions and the B-162 suspensions, respectively, to calculate nebulizer efficiency. Measurements of the P~~L~~SL suspensions were performed with the SP2 laser currents lower than those for rBC measurements. We repeatedly measured the efficiency of the Marin-5 nebulizer system over a ten year period. Additionally, we measured the efficiency of the APEX-Q and U5000AT nebulizer systems. For the APEX-Q nebulizer system, we used two types of nebulizers: the Conikal Nebulizer AR30-1-FC1ES (Glass Expansion, Australia) and the MicroMist U-Series nebulizer AR30-1-UM05E (Glass Expansion, Australia), the latter being the same one used in the Marin-5 nebulizer system.

Number and mass concentrations of rBC particles in the melted ice core samples were calculated using the nebulizer efficiency (Mori et al., 2016). The combination of the Wide-Range SP2 and the Marin-5 nebulizer system provides a measurable diameter range of 70 nm to 4 μm. With this rBC unit attached to the melting and debubbler units, we acquired number concentrations, mass concentrations, and mass equivalent diameters of rBC particles every second. ~~Using the same definition of the detection limit mentioned above (Sect. 2.1), we determined t~~The detection limits of rBC number and mass concentrations in water samples, determined as 3σ of the blank values, ~~to be~~were approximately 10 counts·L^{-1} and 0.01 μg·L^{-1}, respectively. The accuracy of the rBC number and mass concentrations in the water samples was approximately 16%, which was derived from the measurement uncertainties of the peristaltic pump flow rate (±5%), nebulizer flow rate (±5%), nebulizer efficiency (±10%), and rBC concentration in the carrier gas measured by the SP2 (±10%) (Mori et al., 2016, 2021). The reproducibility of the number and mass concentrations for repeated measurements of the same melted ice core and Arctic snow samples on two different days was usually better than 10% (Mori et al., 2019). For example, Mori et al. (2019) demonstrated that the mass and number concentrations of rBC particles in a melted sample from the SIGMA-D core, analysed on the day it was melted and again 21 months later, showed agreement within 5.6% and 4.4%, respectively. Mori et al. (2019) further

demonstrated that the changes in the mass and count median diameters were negligibly small in this sample. Additionally, possible changes in the count median diameter during the nebulizing process were estimated to be only 2 nm for the fullerene soot, whose count median diameter was ~120 nm and whose mass concentration in water was 6.9–64 $\mu g \cdot L^{-1}$ (Mori et al., 2016). A similar value was estimated for the AB-162. These experimental results suggest that the shape of the rBC size distribution and the rBC mass concentration changed little during the nebulizer extraction process.

rBC particles could stick to the various components of the CFA system such as the melt head, debubbler, valves, conductivity cells, tubing, and nebulizer system, which could reduce the concentration and change the size distribution. We investigated whether losses of rBC particles occurred in the CFA system. We injected a melted surface snow sample from SIGMA-A (northwest Greenland) (Matoba et al., 2018) ~~at~~ from above the centre hole of the melt head, and measured the concentration and size distribution of BC particles. We used the University of Copenhagen type melt head for this test. We also injected the same sample directly into the Marin-5 nebulizer system and measured the concentration and size distribution of rBC particles. We then compared the results of the two experiments to check whether any changes occurred that could be attributed to the CFA system.

2.3 Signal dispersion tests

The mixing of meltwater, which occurs in parts of the CFA system such as the melt head, debubbler, valves, conductivity cells, tubing, and nebulizer system, causes signal dispersion and reduces the resolution of the CFA data. To evaluate the signal dispersion, we examined the response of each unit by switching between injection of ultra-pure water and injection of standard solutions or melted ice core/snow samples at the melt heads (Bigler et al., 2011). The ultra-pure water, standard solutions, and melted ice core/snow samples were injected from above the centre hole of the melt heads. The ultra-pure water used in this study was made using a Milli-Q Advantage system (Merck Millipore, Germany). The samples used for the dispersion tests are listed in Table 1.

Table 1. List of samples for signal dispersion tests

Measurement	Type of test samples
rBC	AquaBlack 162 (AB-162, Tokai Carbon Co. Ltd.)

ICP-MS	Surface snow from Dome Fuji, Antarctica, concentrated by heating
~~Water s~~Stable water isotopes	A shallow ice core drilled at Dome Fuji, Antarctica (JARE52 core)

2.4 Processing and analyses of the SIGMA-D ice core

A 222.7 m ice core was drilled at the SIGMA-D site (77.636° N, 59.120° W; 2100 m a.s.l.) in northwest Greenland in spring 2014 (Matoba et al., 2015). The annual mean air temperature and accumulation rate at the site were estimated to be −25.6 °C and 0.23 w eq yr^{-1} (Nagatsuka et al., 2021), respectively. In the field, the top 175.77 m of the core was divided into two vertical sections (Sections A and B).

Section A was kept frozen and transported to NIPR in Japan. We analysed the depth interval between 6.17 and 112.87 m of this section using the CFA system described in Sect. 2.1 and 2.2. The top 6.17 m of this section was too fragile to be analysed with the CFA system; hence, we manually cut segments of approximately 0.1 m. These discrete samples were decontaminated in a cold room (−20 °C) using a precleaned ceramic knife, and then placed in powder-free plastic bags. They were then melted and transferred to precleaned glass and polypropylene bottles in a class 10,000 clean room. The samples in glass bottles were analysed for stable water isotopes and rBC, whereas those in polypropylene bottles were analysed for six elements using an ICP-MS. Analyses of stable water isotopes and six elements are described in Appendix B1. The rBC was analysed using a Wide-Range SP2 (Mori et al., 2016) and a concentric pneumatic nebulizer system (Marin-5, Teledyne CETAC, USA), i.e., the same as those in the NIPR CFA system. The setting and analytical conditions of the Wide-Range SP2 and Marin-5 were similar to those described in Sect. 2.2. Concentrations and diameters of rBC particles were calibrated in the same way as described in Sect. 2.2.

~~Stable isotopes of water for the discrete samples were analysed using a near-infrared cavity ring-down spectrometer (L2120-i, Picarro, Inc. USA), a high-precision vaporizer (A0211, Picarro Inc., USA), and an autosampler (PAL HTC9-xt-LEAP, LEAP Technologies, USA). The precision of determination was ±0.05‰ for $\delta^{18}O$. The samples in polypropylene bottles were analysed for six elements (^{23}Na, ^{24}Mg, ^{27}Al, ^{39}K, ^{40}Ca, and ^{56}Fe) with an ICP-MS (7700 ICP-MS, Agilent Technologies, USA) in a class 10,000 clean room at NIPR.~~

Section B was cut in the field into 0.06–0.12 m long vertical segments for the top 5 m of the core, 0.05–0.08 m long segments for depths of 5–12 m, and approximately 0.05 m long segments for the depth interval between 12 and 112.87 m. Each segment was placed in a plastic bag, melted, and transferred to a precleaned polypropylene bottle in the field. The discrete

samples contained in the polypropylene bottles were refrozen in the field, transported to Japan, and kept frozen until analysis, whereupon they were melted and analysed for major ions and stable water isotopes (Nagatsuka et al., 2021). Analyses of the discrete samples from Section B are described in Appendix B2. ~~Samples from depths above 61.2 m were analysed for Na^+, K^+, Mg^{2+} and Ca^{2+}, Cl^-, NO_3^-, and SO_4^{2-} with two ion chromatographs (ICS-2100, Thermo Fisher Scientific, USA) at Hokkaido University, Japan, whereas samples from depths between 61.2 and 112.87 m were analysed for NH_4^+, Na^+, K^+, Mg^{2+}, Ca^{2+}, Cl^-, NO_3^-, and SO_4^{2-} with two ion chromatographs (ICS-2000, Thermo Fisher Scientific, USA) at NIPR. The limit of detection of Na^+ measured at Hokkaido University was 1 $\mu g \cdot L^{-1}$, and that measured at NIPR was 0.2 $\mu g \cdot L^{-1}$. Stable water isotopes were analysed for all samples from Section B using a near-infrared cavity ring-down spectrometer (L2130-i, Picarro Inc., USA) and a high-throughput vaporizer (A0212, Picarro Inc., USA) at Hokkaido University. The precision of determination was ±0:08‰ for $\delta^{18}O$. For dating purposes, tritium concentrations were measured using a liquid scintillation counter (LSC-LB3; Aloka Co. Ltd., Japan) at 0.05 m intervals for the depth interval of 19.15–26.47 m (Nagatsuka et al., 2021).~~

3 Results and Discussion

3.1 Nebulizer efficiency

Figure 2 shows the efficiency of the Marin-5 nebulizer system for different flow rates of meltwater. As previously reported (Mori et al., 2016), nebulizer efficiency depends on flow rate. For three flow rates—0.19~~2~~, 0.38~~4~~, and 0.4~~7~~8 $mL \cdot min^{-1}$—the efficiency was almost constant for diameters of <2000 nm, and it declined linearly with diameter for diameters >2000 nm, as reported by Mori et al. (2016). For a flow rate of 0.38~~4~~ $mL \cdot min^{-1}$, which is the flow rate used in the NIPR CFA system, the efficiency was 34.2% ± 8.0% for particles with diameter of <2000 nm, and it declined linearly with diameter for diameters of 2–4 µm. The efficiency of Marin-5 was slightly higher than that of APEX-Q for the PSL with diameters between 200 and 700 nm at a flow rate of 0.38 mL min^{-1} (Fig.C1(a)). Repeated measurements of the Marin-5 efficiency over a ten-year period (Fig. 3) indicate that the nebulizer efficiencies remained stable over time, despite some fluctuation around the regression lines. For particles with diameters < 2 µm, the variability was ±8 %, which does not significantly affect the rBC data. Consequently, we applied the same nebulizer efficiency values across all CFA sessions. Additionally, we validated the stability of our WR-SP2/nebulizer system by repeatedly measuring the rBC mass and number concentrations in the same samples, as demonstrated by Mori et al. (2019). In contrast to the Marin-5 nebulizer system, the U5000AT nebulizer system exhibited size- and time-dependent efficiency (Fig. C2(b)).

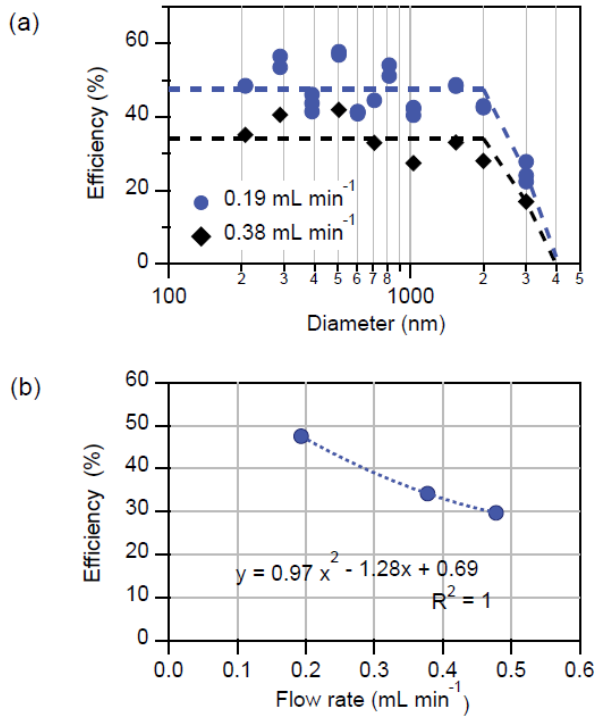

Figure 2: Dependence of Marin-5 nebulizer efficiency on (a) BC diameter for two flow rates and (b) flow rate for BC diameter of <2 µm.

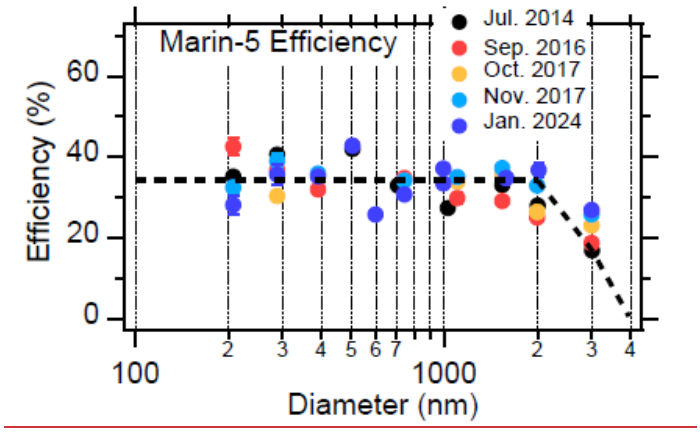

Figure 3: Repeated measurements of Marin-5 nebulizer efficiency over ten years for a flow rate 0.34 mL L^{-1}.

3.2 Signal dispersion

Figure ~~3~~ 4 displays the results of dispersion tests for $\delta^{18}O$, Na, and rBC. We defined two types of response times: (1) the time (t1) required for transition from 10% of the standard (or ice core/snow sample) value to 90% of the standard (or ice core/snow sample) value, and (2) the time (t2) required for transition from 90% of the standard (or ice core/snow sample) value to 10% of the standard (or ice core/snow sample) value. The baseline was determined as the value for Milli-Q water. Response times t1 and t2 depend on how the data are smoothed owing to noise in the data signal. Table 2 shows examples of t1 and t2 when the data are smoothed by taking 5-point running means. Neither t1 nor t2 depends on the standard (or ice core/snow sample) concentrations or values (Bigler et al., 2011). For rBC, we present normalized values together with concentrations in Fig. ~~3~~ 4 to illustrate how we determined t1 and t2. We converted t1 and t2 to depth intervals L1 and L2, respectively, assuming a constant melt speed of 30 mm s^{-1}. In Table 2, we list the averages of L1 and L2 for a rise of 10%–90% and decay of 90%–10%, respectively. L1 and/or L2 are often defined as the depth resolution of a CFA system (Bigler et al., 2011; Erhardt et al., 2023; Grieman et al., 2022). This definition gives a depth resolution of 35-40 mm for the $\delta^{18}O$, Na, and rBC data over the depth interval between 6.17 and 112.87 m. However, the resolution of our CFA system is better than these values suggest. We could resolve two peaks located at distances closer than the resolution defined in this way. For $\delta^{18}O$, Na, and rBC, peaks 10

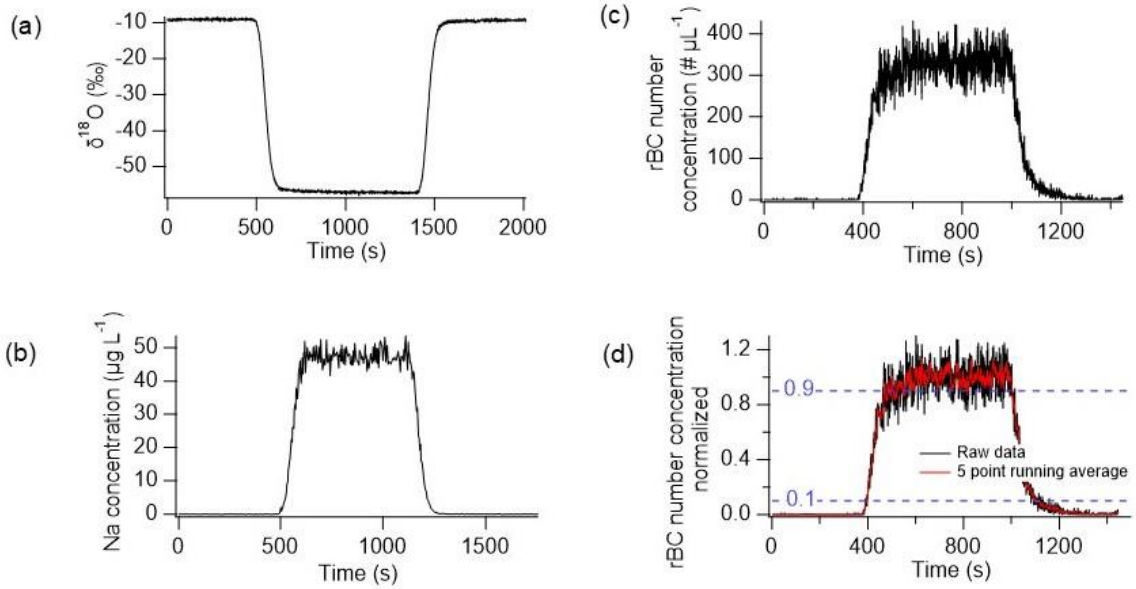

Figure 4: Results of dispersion tests: (a) $\delta^{18}O$, (b) Na concentration, (c) rBC number concentration, and (d) normalized rBC number concentration. Black and red lines represent raw data and 5 point running averages, respectively. Blue dotted lines show 0.1 and 0.9 levels.

mm apart are usually resolved, although peak heights may be slightly reduced for peaks that are less than 35-40 mm apart. For

rBC and Na, L2 is slightly greater than L1, indicating that the melting direction affects the CFA signal (Breton et al., 2012). The CFA signal for rBC and Na might not be symmetrical, even if a concentration peak is symmetrical along the core depth (Breton et al., 2012). Conversely, $\delta^{18}O$ shows similar L1 and L2 values, indicating that melting direction does not affect the CFA signal.

In addition to the mixing that occurs in the debubbler, valves, conductivity cells, tubing, and nebulizer systems, there is also mixing between the meltwater from the center of the ice sample and the meltwater from the ice on outside the inner wall of the melt head. However, due to the very short distance and very small dead volume within the melt head (using a 26 x 26 mm square-shaped melt head as described by Bigler et al. (2011)), this mixing is negligible compared to the mixing that occurs in other parts of the CFA system. Therefore, the signal dispersion observed in this study provides a reliable representation of the dispersion caused by the entire CFA system. Additionally, the stratigraphy of the SIGMA-D core was nearly horizontal, resulting in minimal mixing of ice from different ages.

Table 2 Results of dispersion tests

	University of Copenhagen type melt head					University of Maine type melt head				
	t1 (s)	t2 (s)	L1 (mm)	L2 (mm)	Average of L1 & L2 (mm)	t1 (s)	t2 (s)	L1 (mm)	L2 (mm)	Average of L1 & L2 (mm)
$\delta^{18}O$	78	75	39	37.5	38.3	75	81	37.5	40.5	39
rBC number concentration	67	90	33.5	45	39.3	105	124	52.5	62	57.3
Na concentration	66	74	33	37	35	57	89	28.5	44.5	36.5

3.3 Minimal losses of BC particles in the NIPR CFA system

Figure ~~4~~ 5 and Table 3 present the results of rBC loss tests. The sample injected at the melt head, which then flowed through the CFA system, produced mass and number size distributions of rBC particles consistent with those derived following direct injection. The mass and number concentrations of rBC particles injected at the melt head were 94% and 102% of those determined following direct injection. Thus, the rBC concentrations of the two types of injections agreed within the bounds of uncertainty of the BC measurements. Therefore, we can conclude that minimal loss of rBC particles occurs in the NIPR CFA system. The good agreement between injection at the melt head and the direct injection also supports the reliability and reproducibility of the NIPR CFA-rBC system.

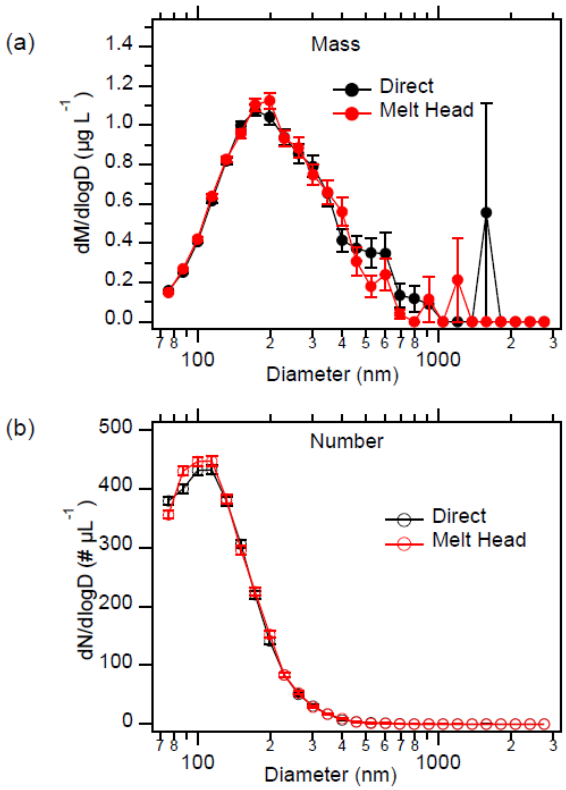

Figure 5~~4~~: Comparison of direct injection of a surface snow sample collected at SIGMA-A to Marin-5 and injection at the melt head. (a) Mass and (b) number size distributions of rBC shown for direct and melt head injections. Error bars indicate $\pm 1\sigma$ of a Poisson distribution.

Table 3 Results of rBC loss test using a surface snow sample from SIGMA-A, northwest Greenland

	Melt head blank	Injection at melt head	Direct injection	Ratio of injection at melt head/direct injection

rBC mass concentration (μg L^{-1})	0.004	0.623	0.660	0.944
rBC number concentration (# L^{-1})	0.1	175.8	173.0	1.016

~~**3.4 Chronology of the SIGMA-D ice core**~~

~~Figure 5a compares the raw $\delta^{18}O$ data obtained from the CFA system and those obtained from the discrete sample analysis. Figure 5b compares the raw Na concentration data obtained from the CFA system using ICP-MS, and the Na^+ concentration data from discrete sample analysis using ion chromatography. The CFA and discrete measurements agree well for $\delta^{18}O$ and Na. The values of Mg, K, and Ca from the CFA analysis (not shown) also agree well with the values of Mg^{2+}, K^+, and Ca^{2+} from the discrete sample analysis, respectively (not shown).~~

~~The CFA data from Section A and the discrete data from Section B agree well, and therefore we adopted the chronology of Section B reported by Nagatsuka et al. (2021) to analyse the BC data from Section A. Because Na^+ (and Na) and $\delta^{18}O$ show regular seasonal peaks in winter and summer, respectively, the dating was based on annual layer counting using mainly Na^+ and $\delta^{18}O$ data from the discrete samples cut from Section B. We also used a tritium peak and volcanic SO_4^{2-} peaks as reference horizons. However, for the years before 1783, we made minor adjustments where high SO_4^{2-} peaks did not match the volcanic eruptions reported following analysis of other Greenland ice cores (Sigl et al., 2018). For the depth intervals where seasonal variability of Na^+ and $\delta^{18}O$ data were ambiguous, we supplementarily used seasonal variability of Ca, which is originated from mineral dust and shows seasonal peaks in late-winter to early spring (e.g., Nakazawa et al., 2021; Kuramoto et al., 2011; Dibb et al., 2007), obtained from the CFA system. The uncertainties of dating were estimated to be less than ±2 years. The CFA data covered the years 1653–2002.~~

3.~~5~~ 4 High-resolution rBC data from the SIGMA-D ice core

Figure 6 displays the raw data of BC mass and number concentrations acquired using the CFA system at 1 s interval corresponding to a depth interval of 0.0005 m, together with the 10 mm averages of the data. The ice-core chronology determined by Nagatsuka et al., (2019) with a slight modification (Goto-Azuma et al., 2024) is shown in Fig. 6. The raw mass concentration data frequently exceeded 50 μg·L^{-1}. However, as can be deduced from the differences in mass concentrations and number concentrations (Fig.6 (a) and (b)) and their enlarged extracts (Fig.6 (c) and (d), respectively), the sporadic high concentration peaks in the raw mass concentration data could have been formed by only a small number of large BC particles, which would result in the noise ~~evident~~ in the data. To reduce the noise, we calculated the 10 mm averages of the data, corresponding to a 1–2 week interval depending on the depth of the core. Averaging the mass concentrations over 10 mm intervals effectively filtered out data noise, while still preserving the large peaks, albeit with slightly reduced amplitudes (Fig. 6(a) and (c)). ~~The 10 mm averages of the mass concentrations~~ The 10 mm averages of the mass concentrations often exceeded

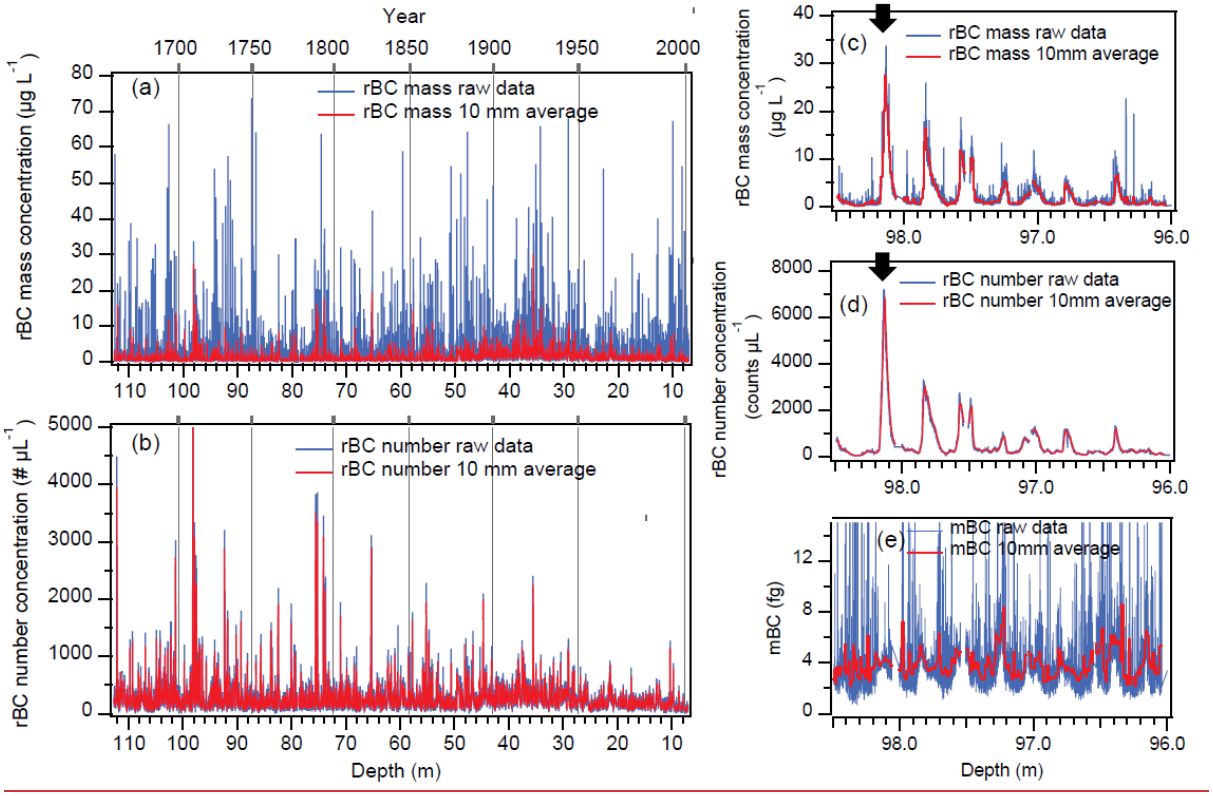

Figure 6: (a) Mass and (b) number concentrations of rBC in the SIGM-D core. (c) and (d) are enlarged extracts of (a) and (b), respectively. (e) mBC (average mass of rBC particles) for the same depth interval as (c) and (d). Raw data and 10 mm averages of the raw data are shown in blue and red, respectively. The arrows (c) and (d) denote the summer of 1710.

10 μg·L^{-1}. The prominent peaks in mass and number concentrations around 98.1 m correspond to the summer of 1710, when rBC particles from a significant biomass burning event were deposited at the SIGMA-D site (Goto-Azuma et al., 2024).

The upper limit of the measurable rBC diameters would affect the rBC mass concentrations if the ice core samples contain a large proportion of large particles. As described in Sect. 2.2, the upper limit of the NIPR rBC unit is 4 μm, whereas ~~that~~ the upper limit of a measurement system using the ~~standard~~off-the-shelf SP2 is ~~850~~ 400-500 nm ~~at best~~ and that of a measurement system using an extended range SP2 and the off-the-shelf SP2-XR is 800-850 nm. If a measurement system uses a nebulizer system such as the U5000AT ultrasonic nebulizer system (Teledyne CETAC, USA), which was used in many previous studies, nebulizer efficiency is drastically reduced for diameters greater than approximately 500 nm (Mori et al., 2016), which would lead to underestimation of rBC mass concentrations if the ice core contains a large proportion of rBC particles with diameter of >500 nm even if an extended range SP2 is used. We calculated the number and mass size distributions of rBC particles averaged over different periods. As an example, the 11-year mean ~~normalized~~ number and mass size

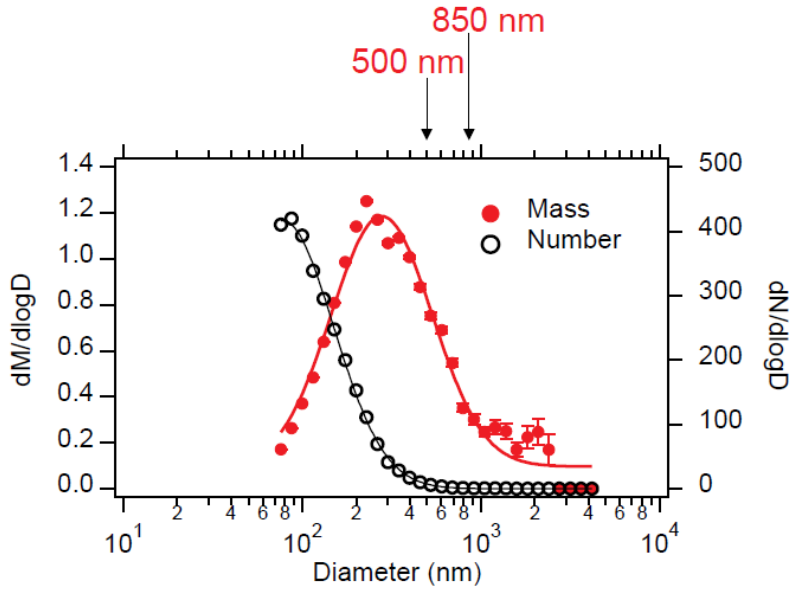

Ratio of rBC mass concentration	Ratio of rBC number concentration	Ratio of rBC mass concentration	Ratio of rBC number concentration
500 nm/Total	500 nm/Total	850 nm/Total	850 nm/Total
0.69	0.99	0.88	1.00

Figure 7: Averaged ~~mass~~ number (black) and ~~number~~ mass (red) size distribution of rBC particles for the period 2003–2013~~, normalized by the averaged total mass and number concentrations~~, respectively. Error bars indicate ±1σ of a Poisson distribution. The table shows ratios of concentrations for upper limits of 500 and 850 nm to total.

distributions for 2003–2013, derived from analyses of the discrete samples, are plotted in Fig. 7. It is evident from Fig. 7 that the total number concentrations of rBC particles would ~~not~~ have been affected little by the upper limits of the measurable BC diameters, which were ~~between~~ approximately ~~600~~ 400-500 nm~~and 850 nm~~ in previous studies and 850-900 nm if an extended range SP2 was used. In contrast, the mass concentrations would have been underestimated by ~~17~~31% and 12% for upper limits of 500 ~~650~~ and 850 nm, respectively.

Figure 8 displays additional examples of mass size distributions of rBC particles for months with significant rBC concentration peaks. Given that the upper limit of measurable rBC diameter is 500 nm, mass concentrations during the summers of 1710 and 1863, and the winters of 1916/17 and 1935/36 would have been underestimated by 8, 43, 26, and 36 %, respectively. The mass size distribution, and consequently the degree of underestimation, varied over time. We calculated the average mass of rBC particles (mBC), by dividing the mass concentration by the number concentration, which serves as one of the rBC size parameters. Fig. 6(e) illustrates an example of the mBC variability with depth, indicating seasonal changes in rBC size distribution. A companion paper (Part 2, Goto-Azuma et al., 2024) further investigated the temporal variability in rBC size distribution. As rBC size distribution changes over time, the underestimation ratio cannot be assumed to be constant. Therefore, it is crucial to extend the measurable rBC diameters beyond 500 nm, desirably beyond 800-850 nm.

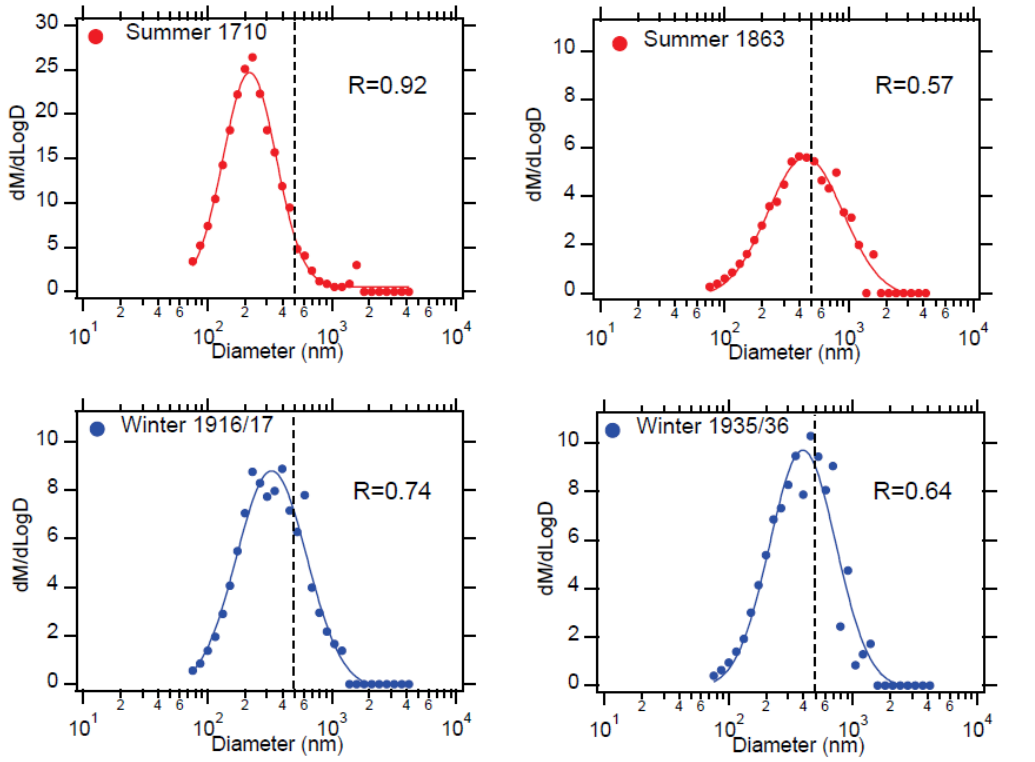

Figure 8: Examples of mass size distributions of rBC particles for summer and winter months showing high rBC concentrations. (a) Summer months of 1710, shown by the arrows in Fig. 6 (a) and (b). (b) Summer months of 1863. (c) Winter months of 1916/17. (d) Winter months of 1935/36. Summer and winter months correspond to approximately May-July and December-February, respectively (Goto-Azuma et al., 2024). The dotted lines show the upper limit of measurable rBC diameter (500 nm) for off-the-shelf SP2. R denotes the ratio of rBC mass concentration for diameter <500 nm to the total rBC mass concentration.

To examine the impact of large rBC particles in the SIGMA-D ice core, the rBC mass concentrations averaged for 10 mm intervals, assuming different upper limits, ~~are~~ were calculated from the size distribution data, and plotted in Fig. ~~8a~~9a. In Fig. ~~8~~9b, the ratios of the rBC mass concentrations for different upper limits versus the total rBC mass concentrations are shown. Figure ~~9~~8b shows that the ~~standard~~ off-the-shelf SP2 combined with a size-independent high-efficiency nebulizer system such as the Marin-5 ~~of~~ or the APEX-Q nebulizer systems, which would give an upper limit of ~~850~~ 500 nm, would occasionally underestimate the rBC mass concentration by ~~10~~30-40% or more. Even an extended range SP2, when combined with a size-independent high-efficiency nebulizer system, could occasionally underestimate the rBC mass concentration by

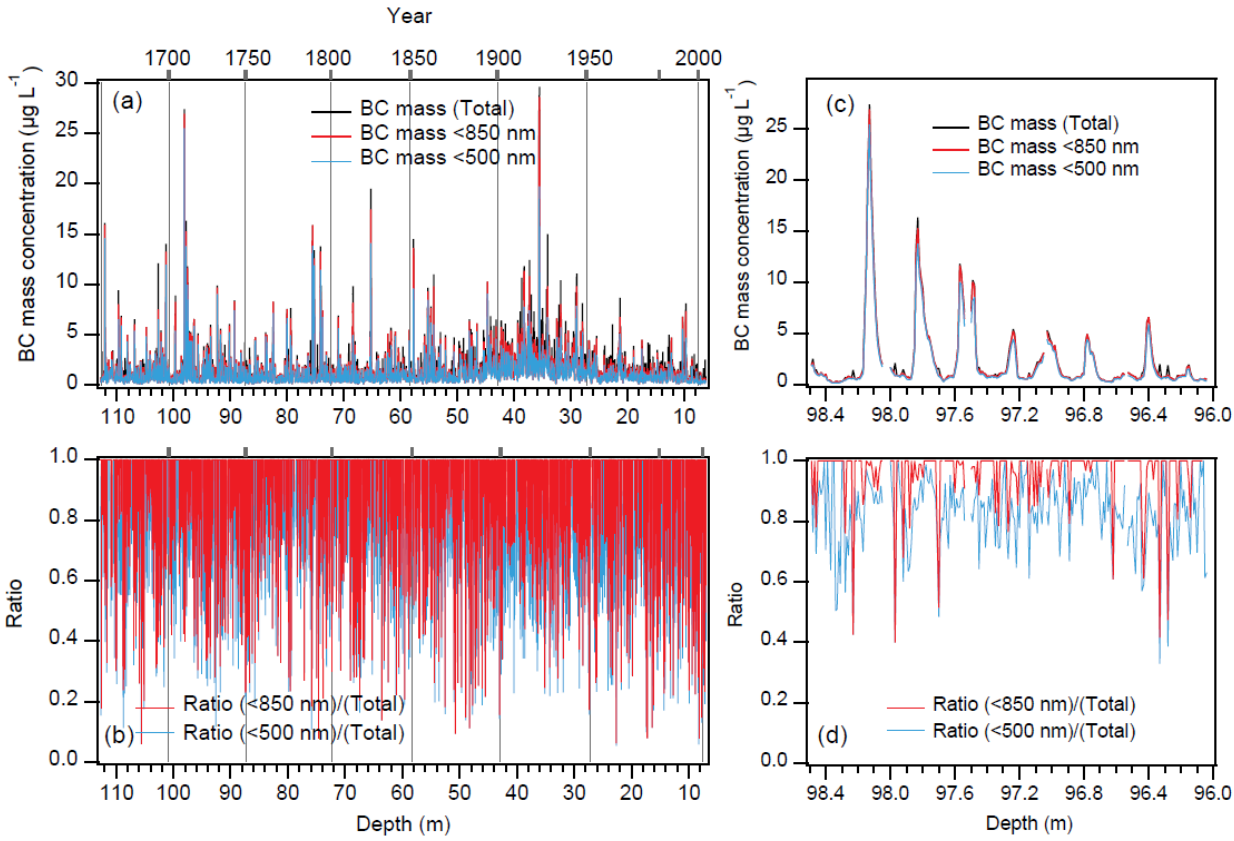

Figure 9: Comparison of rBC mass concentration (10 mm averages) in the SIGMA-D core for different upper limits of measurable rBC diameters. (a) Total concentration measured in this study (upper limit: 4 um), concentration for upper limit of 850 nm, and concentration for upper limit of 500 nm are displayed in black, red, and blue colors, respectively. (b) Ratio of rBC mass concentration for upper limit of 850 nm (red) and 500 nm (blue) to total concentration. (c) and (d) are enlarged extracts of (a) and (b), respectively.

20% or more. ~~However, using a~~If we use ~~a~~ a nebulizer system such as the U5000AT ~~nebulizer~~, ~~whose efficiency depends substantially on the diameter of BC particles, the upper limit would be approximately 600–650 nm, and we would frequently underestimate the BC mass concentration by 80% or more~~underestimation would be even greater, though difficult to quantify due to its size- and time- dependent efficiency. Figure ~~9~~10 presents histograms of the ratios of rBC mass concentrations for upper limits of ~~650~~ 500 and 850 nm. For the upper limit of ~~650~~ 500 nm, ~~36~~67% of the 10 mm averages account for <90% of the total rBC mass concentrations; whereas for the upper limit of 850 nm, 15% of the 10 mm averages account for <90% of the total rBC mass concentrations.

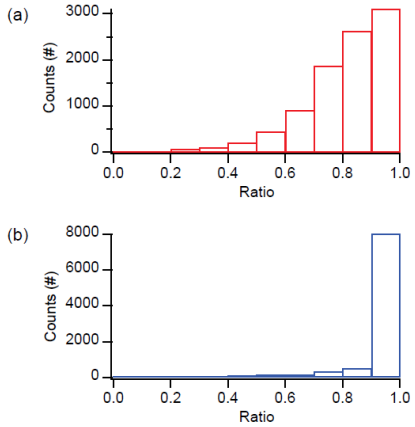

Figure 10: Histograms of underestimation for 10 mm averaged data. Horizontal axis represents the ratio of mass concentration for an upper limit of (a) 500 nm and (b) 850 nm. Vertical axis represents the number of 10 mm averaged data in each ratio bin.

4. Conclusions

We developed a CFA system and incorporated an rBC unit that uses the improved rBC measurement technique developed by Mori et al. (2016). The CFA system can acquire continuous and high-resolution measurements of the number and mass concentrations of rBC, and the size distribution of rBC particles, in addition to stable water isotopes ($\delta^{18}O$ and δD), six elements (^{23}Na, ^{24}Mg, ^{27}Al, ^{39}K, ^{43}Ca, and ^{56}Fe), microparticles, electrical conductivity, and methane. There were minimal losses of rBC particles within the NIPR CFA system. We analysed the SIGMA-D ice core retrieved from northwest Greenland using this newly developed system. If we define the depth resolution as the average of the rise of 10%–90% and decay of 90%–10% of the CFA signal, the resolutions were 38, 39, and 35 mm for $\delta^{18}O$, rBC, and Na, respectively. These depth resolutions correspond to the temporal resolutions of 0.08–0.16, 0.11–0.23, and 0.07–0.15 years for $\delta^{18}O$, rBC, and Na, respectively, depending on depth. However, we could usually resolve two peaks that were approximately 10 mm apart, corresponding to ~~0.5–1.0~~1-2 weeks depending on depth. We were able to analyse monthly resolved rBC data as described in the companion paper, i.e., Part 2 of our study on rBC in the SIGMA-D core (Goto-Azuma et al., 2024).

The Wide-Range SP2 and the Marin-5 nebulizer system allowed analysis of rBC particles with diameter between approximately 70 nm and 4 μm, contrasting with the analysis of rBC particles with diameter of between 70 and ~~600~~400-500~~–850~~ nm reported in previous ice-core studies. This enabled us to reconstruct accurate mass concentrations and size distributions of rBC particles, together with their temporal changes (Goto-Azuma et al., ~~submitted~~2024), which could contribute to estimation of the impacts of rBC on the radiation budget and cloud microphysics. Using the size distribution data, we estimated the extent of underestimation that would result from using~~be caused by~~ (1) an off-the-shelf~~combination of the standard~~ traditional SP2, which can measure rBC particles with diameters <500nm,~~ and a high efficiency nebulizer~~, and (2) an ~~combination of the standard~~ SP2 modified by Moteki and Kondo (2011) or an off-the-shelf SP2-XR which can measure rBC particles with diameter <850 nm. In both cases, we assumed size-independent efficiency for nebulizer systems such as the Marin-5 and the APEX-Q~~and a traditional ultrasonic nebulizer~~. For (1), approximately ~~15~~67% and 37 % of the 10 mm averaged data from the SIGMA-D core accounted for <90% and <80% of the total rBC mass concentrations, respectively. For (2), approximately ~~36~~15% and 10% of the 10 mm averaged data from the SIGMA-D core accounted for <90% and <80% of the total rBC mass concentrations, respectively. The extent of the underestimation depends on depth and thus on the age of the core. For the period 2003–2013, (1) and (2) would lead to underestimation of the averaged mass concentration by 31~~12~~% and 12~~17~~%, respectively. For large concentration peaks resulting from significant boreal forest fires and anthropogenic inputs, underestimation would frequently exceed 40%.

Although few ice core studies have considered the size distribution of rBC and estimated the extent of underestimation of rBC mass concentrations, the present-day snow from Svalbard (Mori et al., 2019) and an ice core from Mt. Elbrus in the western Caucasus Mountains (Lim et al., 2017) do contain non-negligible amounts of rBC particles with diameter of >~~650~~ 500 nm or 850 nm. Since the size distributions do not always follow the lognormal distributions~~Therefore~~, the improved method for accurate measurement of rBC mass concentrations should be ~~used~~ employed to properly constrain aerosol models.

Appendix A: Details of the NIPR CFA system

An ice core sample (cross section: 34 mm × 34 mm, length: ~0.5 m) was placed on a melt head inside a freezer. An 850 g weight was placed on top of the ice sample to allow stable melting. Before the ice core sample was completely melted, another similarly sized ice core sample was stacked on top of the first sample to maintain continuous melting of the ice samples. To promote melting, heaters are inserted into the melt head (Bigler et al., 2011; Osterberg et al., 2006). In the earlier NIPR

CFA system, we used a melt head developed at the University of Maine (Osterberg et al., 2006). However, in this study, we used a melt head similar to the one ~~used~~developed at the University of Copenhagen by Bigler et al. (2011) for the depth interval between 11.3 and 112.8 m of the SIGMA-D core. The University of Maine type melt head, designed principally for use in firn core analyses, is not airtight. For methane analysis, we had to use an airtight melt head such as the one used by Bigler et al. (2011). For the depth interval between 6.17 and 11.3 m of the SIGMA-D core, we used the University of Maine type melt head (Dallmayr et al., 2016; Osterberg et al., 2006) to reduce water percolation through the porous firn caused by capillary action (Osterberg et al., 2006). For depths < 49.3 m, methane measurement was not performed.

The depth of an ice core sample was assigned using a laser positioning sensor (LKG-G505, Keyence, Japan), which determined the distance from the sensor to the top of the weight (Dallmayr et al., 2016). A typical melt speed, regulated by the voltage applied to the heaters in the melt head, was 30 mm min^{-1}. The depth resolution of the laser positioning sensor with this melt speed was approximately 0.3 ± 0.1 mm. The meltwater collected in the contamination-free inner part of the melt head is drawn through perfluoroalkoxy alkane tubing, an injection valve, and the debubbler unit by a peristaltic pump (Minipuls3 MP-2, Gilson, USA). Following removal of air bubbles by the debubbler unit, the meltwater is introduced to the different measurement units and to the fraction collector unit using peristaltic pumps (Reglo Digital ISM596, ISMATEC, Germany). Before each unit, an electrical conductivity cell (conductivity meter Model 1056, Amber Science Inc., USA) is placed as close as possible to the unit to synchronise the depths of the ice core data acquired by the different measurement units and the depths of the meltwater samples collected by the fraction collector unit (McConnell et al., 2002; Dallmayr et al., 2016). A length of approximately 7 m of the ice core was melted once or twice a week. The lengths of the tubing between (1) the melt head and the debubbler, (2) the debubbler and the ICP-MS unit, (3) the debubbler and the water istotope unit, and (4) the debubbler and the rBC unit were approximately 1 m, 3 m, 1.2 m, and 1.5m, respectively. The inner diameters of the tubing for the ICP-MS unit, water isotope unit, and rBC unit were 0.03, 0.02, and 0.03 inches, respectively.

The ICP-MS unit consists of an ICP-MS (7700 ICP-MS, Agilent Technologies, USA) including a nebulizer system. The elements ^{23}Na, ^{24}Mg, ^{27}Al, ^{39}K, ^{43}Ca, and ^{56}Fe were each measured at a 3.00 s interval. Additionally, ^{89}Y was measured at a 3.00 s interval to check the stability of the ICP-MS. Data acquisition times for ^{23}Na, ^{24}Mg, ^{27}Al, ^{39}K, ^{43}Ca, ^{56}Fe, and ^{89}Y were 0.02, 0,1, 0.2, 0.1, 2.27, 0.252, and 0.044 s, respectively. We used mainly ^{23}Na data to date the core. The concentration of each of the elements was calibrated both before and after the CFA measurements of the day using a multi-element standard solution (XSTC-331, Spex CertiPrep, USA) diluted with ultra-pure water (Milli-Q water, Milli-Q Advantage, Merck

Millipore, Germany). The detection limit, defined as [3σ of the blank value + the intercept of the calibration line], of ^{23}Na is 0.5 µg L^{-1}.

The stable water isotope unit is essentially same as that used by Dallmayr et al. (2016). It consists of a vaporization module (Gkinis et al., 2011; Dallmayr et al., 2016), and a wavelength-scanned cavity ring-down spectrometer (L2130-i or L2120-i, Picarro Inc., USA). The Picarro L2130-i was used for the depth interval between 107.3 and 49.3 m, while the Picarro L2120-I was used for the remaining depths. We calibrated the spectrometer by analysing three sets of laboratory water isotope standards after the CFA measurements of the day. These laboratory standards were calibrated with VSMOW2 and SLAP2 standards purchased from the International Atomic Energy Agency. Details of calibrations and the performance of the stable water isotope unit have been described in a previous study (Dallmayr et al., 2016). Both the L2130-i and L2120-i demonstrated sufficient stability during the 4-5 hours of a daily CFA session, confirmed by Mill-Q water runs before and after the CFA measurements. The good agreement between the CFA data (from Section A of the SIGMA-D core) and discrete sample data (from Section B of the core) also confirms the stability of both Picarros (Goto-Azuma et al., 2024).

Appendix B: Analyses of discrete samples

B1 Discrete samples from Section A of SIGMA-D core

From the top 6.17 m of Section A of the SIGMA-D core, discrete samples were prepared (Sect. 2.4). The samples in glasss bottles were analysed for ~~S~~stable isotopes of water ~~for the discrete samples were analysed~~ using a near-infrared cavity ring-down spectrometer (L2120-i, Picarro, Inc. USA), a high-precision vaporizer (A0211, Picarro Inc., USA), and an autosampler (PAL HTC9 - xt - LEAP, LEAP Technologies, USA). The precision of determination was ±0~~:~~.05‰ for $\delta^{18}O$. The samples in polypropylene bottles were analysed for six elements (^{23}Na, ^{24}Mg, ^{27}Al, ^{39}K, ^{40}Ca, and ^{56}Fe) with an ICP-MS (7700 ICP-MS, Agilent Technologies, USA) in a class 10,000 clean room at NIPR.

B2 Discrete samples from Section B of SIGMA-D core

Samples from depths above 61.2 m were analysed for Na^+, K^+, Mg^{2+} and Ca^{2+}, Cl^-, NO_3^-, and SO_4^{2-} with two ion chromatographs (ICS-2100, Thermo Fisher Scientific, USA) at Hokkaido University, Japan, whereas samples from depths between 61.2 and 112.87 m were analysed for NH_4^+, Na^+, K^+, Mg^{2+}, Ca^{2+}, Cl^-, NO_3^-, and SO_4^{2-} with two ion chromatographs (ICS-2000, Thermo Fisher Scientific, USA) at NIPR. The limit of detection of Na^+ measured at Hokkaido University was 10

μg·L^{-1}, and that measured at NIPR was 0.2 μg·L^{-1}. Stable water isotopes were analysed for all samples from Section B using a near-infrared cavity ring-down spectrometer (L2130-i, Picarro Inc., USA) and a high-throughput vaporizer (A0212, Picarro Inc., USA) at Hokkaido University. The precision of determination was ±0. 1 ‰ for $\delta^{18}O$. The good agreement between the CFA data and discrete sample data from Sections A and B, respectively, ensured the high quality of the CFA data. For dating purposes, tritium concentrations were measured using a liquid scintillation counter (LSC-LB3; Aloka Co. Ltd., Japan) at 0.05 m intervals for the depth interval of 19.15–26.47 m (Nagatsuka et al., 2021).

Appendix C

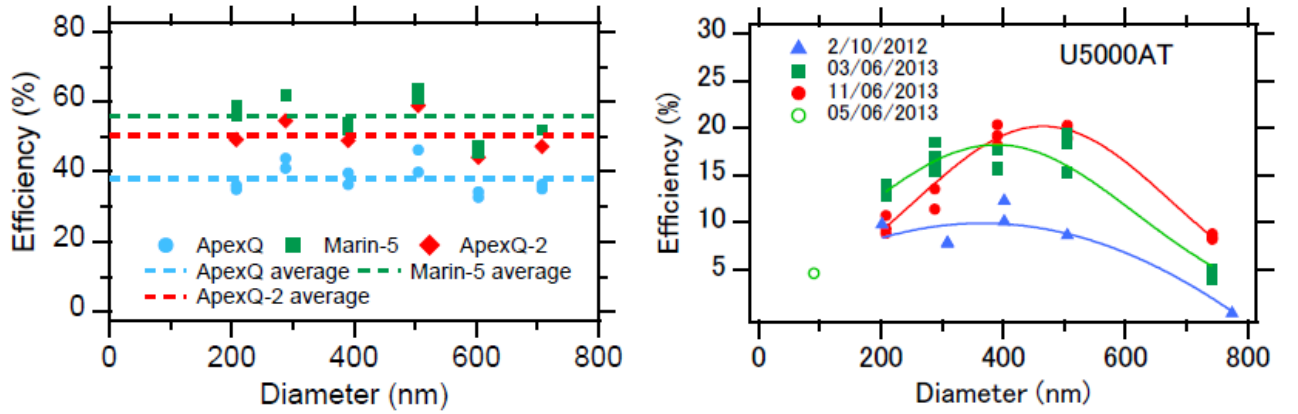

Figure C1: (a) Comparison of Marin-5 and APEX-Q nebulizer efficiency for a flow rate of 0.19 mL min^{-1}. A MicroMist U-series AR30-1-UM05E (Glass Expansion, Australia) was used for the Marin-5 nebulizer system. On the other hand, two types of nebulizers, a Conikal Nebulizer AR30-1-FC1ES (Glass Expansion, Australia) and a MicroMist U-Series nebulizer AR30-1-UM05E (Glass Expansion, Australia) were used for the Apex-Q nebulizer system. ApexQ and ApexQ2 represent the APEX-Q nebulizer system used with the former and the latter nebulizers, respectively. (b) Repeated measurements of efficiency of U5000AT nebulizer system for a flow rate of 0.19 mL min^{-1}.

Data availability

The data used in this study will be submitted to the Arctic Data Archive System when the manuscript has been published.

Author contributions

KGA designed the study and led the manuscript writing. RD, MH, KGA, and KeK built the CFA system at NIPR. NM, TM, SO, YK, and MK developed the improved method for rBC analyses, including the calibration method. YOT, RD, JO, and KyK performed the CFA analyses of the SIGMA-D core. YOT measured nebulizer efficiencies and performed rBC loss tests. YOT, JO and MH performed dispersion tests. SM, KoF, NN, and AT dated the core. KGA, YOT, and KaF analysed the CFA data. MH and SM measured ion concentrations. TA designed and led the ice coring project at SIGMA-D. All the authors discussed the results.

Competing interests

The authors declare that they have no conflict of interest.

Acknowledgements

We would like to thank Hideaki Motoyama for drilling the SIGMA-D core and Yuki Komuro for cutting and processing the core in the field. We also express our gratidude to Kazuhiro Hayashi for assisting with the dispersion tests. We are grateful to the University of Copenhagen and the University of Maine for providing the melt head designs. We acknowledge Margit Schwikowski and Joe McConnell for their valuable advice in developing the CFA-rBC system at NIPR. Additionally, we appreciate the helpful comments from the three anonymous reviewers. ~~We would like to thank Hideaki Motoyama who drilled the SIGMA-D core, and Yuki Komuro who cut and processed the core in the field. We would also like to thank Kazuhiro Hayashi who assisted the dispersion tests. We are grateful to the University of Copenhagen and the University of Maine for providing us with the melt head designs.~~ This study has been supported by the JSPS KAKENHI (Grant Numbers: JP 22221002, JP23221004, and JP18H04140), the Arctic Challenge for Sustainability (ArCS) Project (Program Grant Number: JPMXD130000000)), the Arctic Challenge for Sustainability II (ArCS II) Project (Program Grant Number: JPMXD1420318865), and the Environment Research and Technology Development Funds (JPMEERF20172003, JPMEERF20202003 and JPMEERF20232001) of the Environmental Restoration and Conservation Agency of Japan. We thank James Buxton MSc, from Edanz (https://jp.edanz.com/ac), for editing a draft of this manuscript.

References

AMAP: Arctic Climate Change Update 2021: Key Trends and Impacts, Summary for Policy-makers, 2021.

Arienzo, M. M., McConnell, J. R., Murphy, L. N., Chellman, N., Das S., Kipfstuhl, S., and Mulvaney, R.: Holocene black carbon in Antarctica paralleled Southern Hemisphere climate, J. Geophys. Res.-Atmos., 122, 6713 - 6728, doi:10.1002/2017JD026599, 2019.

Baumgardner, D.: Warming of the Arctic lower stratosphere by light absorbing particles, Geophys. Res. Lett., 31, 10.1029/2003gl018883, 2004.

Baumgardner, D., Kok, G., and Raga, G.: Warming of the Arctic lower stratosphere by light absorbing particles, Geophys. Res. Lett., 31, https://doi.org/10.1029/2003GL018883, 2004.

Bigler, M., Svensson, A., Kettner, E., Vallelonga, P., Nielsen, M. E., and Steffensen, J. P.: Optimization of high-resolution continuous flow analysis for transient climate signals in ice cores, Environ. Sci. Technol., 45, 4483–4489, 10.1021/es200118j, 2011.

Bisiaux, M. M., Edwards, R., McConnell, J. R., Albert, M. R., Anschütz, H., Neumann, T. A., Isaksson, E., and Penner, J. E.: Variability of black carbon deposition to the East Antarctic Plateau, 1800–2000 AD, Atmos. Chem. Phys., 12, 3799–3808, 10.5194/acp-12-3799-2012, 2012a.

Bisiaux, M. M., Edwards, R., McConnell, J. R., Curran, M. A. J., Van Ommen, T. D., Smith, A. M., Neumann, T. A., Pasteris, D. R., Penner, J. E., and Taylor, K.: Changes in black carbon deposition to Antarctica from two high-resolution ice core records, 1850–2000 AD, Atmos. Chem. Phys., 12, 4107–4115, 10.5194/acp-12-4107-2012, 2012b.

Bond, T. C., Doherty, S. J., Fahey, D. W., Forster, P. M., Berntsen, T., DeAngelo, B. J., Flanner, M. G., Ghan, S., Kärcher, B., Koch, D., Kinne, S., Kondo, Y., Quinn, P. K., Sarofim, M. C., Schultz, M. G., Schulz, M., Venkataraman, C., Zhang, H., Zhang, S., Bellouin, N., Guttikunda, S. K., Hopke, P. K., Jacobson, M. Z., Kaiser, J. W., Klimont, Z., Lohmann, U., Schwarz, J. P., Shindell, D., Storelvmo, T., Warren, S. G., and Zender, C. S.: Bounding the role of black carbon in the climate system: A scientific assessment, J. Geophys. Res.-Atmos., n/a-n/a, 10.1002/jgrd.50171, 2013.

Breton, D. J., Koffman, B. G., Kurbatov, A. V., Kreutz, K. J., and Hamilton, G. S.: Quantifying signal dispersion in a hybrid ice core melting system, Environ. Sci. Technol., 46, 11922–11928, 10.1021/es302041k, 2012.

~~Brown, P. T., Hanley, H., Mahesh, A., Reed, C., Strenfel, S. J., Davis, S. J., Kochanski, A. K., and Clements, C. B.: Climate warming increases extreme daily wildfire growth risk in California, Nature, 621, 760–766, 10.1038/s41586-023-06444-3, 2023.~~

Dallmayr, R., Goto-Azuma, K., Kjær, H. A., Azuma, N., Takata, M., Schüpbach, S., and Hirabayashi, M.: A high-resolution continuous flow analysis system for polar ice cores, B. Glaciol. Res., 34, 11–20, 10.5331/bgr.16R03, 2016.

Dibb, J. E., Whitlow, S. I., and Arsenault, M.: Seasonal variations in the soluble ion content of snow at Summit. Greenland: Constraints from three years of daily surface snow samples, Atmos. Environ., 41, 5007–5019, 10.1016/j.atmosenv.2006.12.010, 2007.

Du, Z.-H., Xiao, C.-D., Dou, T.-F., Li, C.-J., Ding, M.-H., Sharma, S., Ma, X.-Y., Wang, S.-M., and Zhang, W.-B.: A shallow ice core from East Greenland showing a reduction in black carbon during 1990–2016, Adv. Clim. Change Res., 11, 360–369, https://doi.org/10.1016/j.accre.2020.11.009, 2020.

Erhardt, T., Jensen, C. M., Adolphi, F., Kjær, H. A., Dallmayr, R., Twarloh, B., Behrens, M., Hirabayashi, M., Fukuda, K., Ogata, J., Burgay, F., Scoto, F., Crotti, I., Spagnesi, A., Maffezzoli, N., Segato, D., Paleari, C., Mekhaldi, F., Muscheler, R., Darfeuil, S., and Fischer, H.: High-resolution aerosol data from the top 3.8-kyr of the East Greenland Ice coring Project (EGRIP) ice core, Earth Syst. Sci. Data, 15, 5079–5091, 10.5194/essd-15-5079-2023, 2023.

Gkinis, V., Popp, T. J., Blunier, T., Bigler, M., Schupbach, S., Kettner, E., and Johnsen, S. J.: Water isotopic ratios from a continuously melted ice core sample, Atmos. Meas. Tech., 4, 2531–2542, 10.5194/amt-4-2531-2011, 2011.

Goto-Azuma, K., Ogawa-Tsukagawa, Y., Fukuda, K., Fujita, K., Hirabayashi, M., Dallmayr, R., Ogata, J, Moteki, N., Mori, T., Ohata, S., Kondo, Y., Koike6, M., Matoba, S., and Aoki, T.: High-resolution analyses of concentrations and sizes of black carbon particles deposited on northwest Greenland over the past 350 years - Part 2: Seasonal and temporal trends in black carbon originated from fossil fuel combustion and biomass burning, EGUsphere, https://doi.org/10.5194/egusphere-2024-1498, 2024.

Grieman, M. M., Hoffmann, H. M., Humby, J. D., Mulvaney, R., Nehrbass-Ahles, C., Rix, J., Thomas, E. R., Tuckwell, R., and Wolff, E. W.: Continuous flow analysis methods for sodium, magnesium, and calcium detection in the Skytrain ice core, J. Glaciol., 68, 90–100, 10.1017/jog.2021.75, 2022.

Kaspari, S. D., Schwikowski, M., Gysel, M., Flanner, M. G., Kang, S., Hou, S., and Mayewski, P. A.: Recent increase in black carbon concentrations from a Mt. Everest ice core spanning 1860–2000 AD, Geophys. Res. Lett., 38, L04703, 10.1029/2010gl046096, 2011.

Keane, R. E., Agee, J. K., Fulé, P., Keeley, J. E., Key, C., Kitchen, S. G., Miller, R., and Schulte, L. A.: Ecological effects of large fires on US landscapes: benefit or catastrophe?, Int. J. Wildland Fire, 17, 696–712, https://doi.org/10.1071/WF07148, 2008.

Keeley, J. E. and Syphard, A. D.: Large California wildfires: 2020 fires in historical context, Fire Ecol., 17, 22, 10.1186/s42408-021-00110-7, 2021.

Kinase, T., Adachi, K., Oshima., N., Goto-Azuma, K., Ogawa-Tsukagawa, Y., Kondo, Y., Moteki, N., Ohata, S., Mori, T., Hayashi, M., Hara, K., Kawashima, J., and Kita, K.: Concentrations and size distributions of black carbon in the surface snow of Eastern Antarctica in 2011. J. Gephys. Res.-Atmos., 125, e2019JD030737. https://doi.org/10.1029/2019JD030737, 2020.

Kuramoto, T., Goto-Azuma, K., Hirabayashi, M., Miyake, T., Motoyama, H., Dahl-Jensen, D., and Steffensen, J. P.: Seasonal variations of snow chemistry at NEEM, Greenland, Ann. Glaciol., 52, 193–200, 10.3189/172756411797252365, 2011.

Lim, S., Faïn, X., Zanatta, M., Cozic, J., Jaffrezo, J.-L., Ginot, P., and Laj, P.: Refractory black carbon mass concentrations in snow and ice: method evaluation and inter-comparison with elemental carbon measurement, Atmos. Meas. Tech., 7, 3307-3324. doi: 10.5194/amt-7-3307-2014, 2014.

Lim, S., Faïn, X., Ginot, P., Mikhalenko, V., Kutuzov, S., Paris, J. D., Kozachek, A., and Laj, P.: Black carbon variability since preindustrial times in the eastern part of Europe reconstructed from Mt. Elbrus, Caucasus, ice cores, Atmos. Chem. Phys., 17, 3489–3505, 10.5194/acp-17-3489-2017, 2017.

Matoba, S., Motoyama, H., Fujita, K., Yamasaki, T., Minowa, M., Onuma, Y., Komuro, Y., Aoki, T., Yamaguchi, S., Sugiyama, S., and Enomoto, H.: Glaciological and meteorological observations at the SIGMA-D site, northwestern Greenland Ice Sheet, B. Glaciol. Res., 33, 7‑14, 10.5331/bgr.33.7, 2015.

Matoba, S., Niwano, M., Tanikawa, T., Iizuka, Y., Yamasaki, T., Kurosaki, Y., Aoki, T., Hashimoto, A., Hosaka, M., and Sugiyama, S.: Field activities at the SIGMA-A site, northwestern Greenland Ice Sheet, 2017, B. Glaciol. Res., 36, 15–22, 10.5331/bgr.18R01, 2018.

Matsui, H.: Development of a global aerosol model using a two-dimensional sectional method: 1. Model design, J. Adv. Model. Earth Syst., 9, 1921‑1947, doi:10.1002/2017MS000936, 2017.

652 Matsui, H. and Mahowald, N.: Development of a global aerosol model using a two-dimensional sectional method: 2.
653 Evaluation andsensitivity simulations, J. Adv. Model. Earth Syst., 9, 1887‑1920, doi:10.1002/2017MS000937, 2017.
654 Matsui, H., Mori, T., Ohata, S., Moteki, N., Oshima, N., Goto-Azuma, K., Koike, M., and Kondo, Y.: Contrasting source
655 contributions of Arctic black carbon to atmospheric concentrations, deposition flux, and atmospheric and snow radiative
656 effects, Atmos. Chem. Phys., 22, 8989–9009, 10.5194/acp-22-8989-2022, 2022.
657 McConnell, J. R., Lamorey, G. W., Lambert, S. W., and Taylor, K. C.: Continuous ice-core chemical analyses using inductively
658 coupled plasma mass spectrometry, Environ. Sci. Technol., 36, 7–11, 10.1021/es011088z, 2002.
659 McConnell, J. R., Edwards, R., Kok, G. L., Flanner, M. G., Zender, C. S., Saltzman, E. S., Banta, J. R., Pasteris, D. R., Carter,
660 M. M., and Kahl, J. D.: 20th-century industrial black carbon emissions altered Arctic climate forcing, Science, 317, 1381–
661 1384, 10.1126/science.1144856, 2007.
662 Mori, T., Moteki, N., Ohata, S., Koike, M., Goto-Azuma, K., Miyazaki, Y., and Kondo, Y.: Improved technique for measuring
663 the size distribution of black carbon particles in liquid water, Aerosol Sci. Tech., 50, 242–254,
664 10.1080/02786826.2016.1147644, 2016.
665 Mori, T., Goto-Azuma, K., Kondo, Y., Ogawa-Tsukagawa, Y., Miura, K., Hirabayashi, M., Oshima, N., Koike, M., Kupiainen,
666 K., Moteki, N., Ohata, S., Sinha, P. R., Sugiura, K., Aoki, T., Schneebeli, M., Steffen, K., Sato, A., Tsushima, A., Makarov,
667 V., Omiya, S., Sugimoto, A., Takano, S., and Nagatsuka, N.: Black carbon and inorganic aerosols in Arctic snowpack, J.
668 Geophys. Res.-Atmos., 124, 13325–13356, 10.1029/2019jd030623, 2019.
669 Mori, T., Kondo, Y., Ohata, S., Goto-Azuma, K., Fukuda, K., Ogawa-Tsukagawa, Y., Moteki, N., Yoshida, A., Koike, M.,
670 Sinha, P. R., Oshima, N., Matsui, H., Tobo, Y., Yabuki, M., and Aas, W.: Seasonal variation of wet deposition of black
671 carbon at Ny-Ålesund, Svalbard, J. Geophys. Res.-Atmos., 126, e2020JD034110, https://doi.org/10.1029/2020JD034110,
672 2021.
673 Moteki, N.: Climate-relevant properties of black carbon aerosols revealed by in situ measurements: a review, Prog. Earth
674 Planet. Sci., 10, 12, 10.1186/s40645-023-00544-4, 2023.
675 Moteki, N. and Kondo, Y.: Dependence of laser-induced incandescence on physical properties of black carbon aerosols:
676 Measurements and theoretical interpretation, Aerosol Sci. Tech., 44, 663–675, 10.1080/02786826.2010.484450, 2010.
677 Nagatsuka, N., Goto-Azuma, K., Tsushima, A., Fujita, K., Matoba, S., Onuma, Y., Dallmayr, R., Kadota, M., Hirabayashi, M.,
678 Ogata, J., Ogawa-Tsukagawa, Y., Kitamura, K., Minowa, M., Komuro, Y., Motoyama, H., and Aoki, T.: Variations in

mineralogy of dust in an ice core obtained from northwestern Greenland over the past 100 years, Clim. Past, 17, 1341–1362, 10.5194/cp-17-1341-2021, 2021.

Nakazawa, F., Nagatsuka, N., Hirabayashi, M., Goto-Azuma, K., Steffensen, J. P., and Dahl-Jensen, D.: Variation in recent annual snow deposition and seasonality of snow chemistry at the east Greenland ice core project (EGRIP) camp, Greenland, Polar Sci., 27, 100597, https://doi.org/10.1016/j.polar.2020.100597, 2021.

Ohata, S., Moteki, N., and Kondo, Y.: Evaluation of a method for measurement of the concentration and size distribution of black carbon particles suspended in rainwater, Aerosol Sci. Tech., 45, 1326–1336, 10.1080/02786826.2011.593590, 2011.

Ohata, S., Moteki, N., Schwarz, J., Fahey, D., and Kondo, Y.: Evaluation of a method to measure black carbon particles suspended in rainwater and snow samples, Aerosol Sci. Technol., 47, 1073–1082, 10.1080/02786826.2013.824067, 2013.

Osmont, D., Wendl, I. A., Schmidely, L., Sigl, M., Vega, C. P., Isaksson, E., and Schwikowski, M.: An 800-year high-resolution black carbon ice core record from Lomonosovfonna, Svalbard, Atmos. Chem. Phys., 18, 12777–12795, 10.5194/acp-18-12777-2018, 2018.

Osterberg, E. C., Handley, M. J., Sneed, S. B., Mayewski, P. A., and Kreutz, K. J.: Continuous ice core melter system with discrete sampling for major ion, trace element, and stable isotope analyses, Environ. Sci. Technol., 40, 3355–3361, 10.1021/es052536w, 2006.

Petzold, A., Ogren, J. A., Fiebig, M., Laj, P., Li, S.-M., Baltensperger6, U., Holzer-Popp, T., Kinne, S., Pappalardo, G., Sugimoto, N., Wehrli, C., Wiedensohler, A., and Zhang, X.-Y.: Recommendations for reporting “black carbon” measurements, Atmos. Chem. Phys., 13, 8365–8379, 10.5194/acp-13-8365-2013, 2013.

Rantanen, M., Karpechko, A. Y., Lipponen, A., Nordling, K., Hyvärinen, O., Ruosteenoja, K., Vihma, T., and Laaksonen, A.: The Arctic has warmed nearly four times faster than the globe since 1979, Commun. Earth Environ., 3, 168, 10.1038/s43247-022-00498-3, 2022.

Schwarz, J. P., Gao, R. S., Fahey, D. W., Thomson, D. S., Watts, L. A., Wilson, J. C., Reeves, J. M., Darbeheshti, M., Baumgardner, D. G., Kok, G. L., Chung, S. H., Schulz, M., Hendricks, J., Lauer, A., Kärcher, B., Slowik, J. G., Rosenlof, K. H., Thompson, T. L., Langford, A. O., Loewenstein, M., and Aikin, K. C.: Single-particle measurements of mid-latitude black carbon and light-scattering aerosols from the boundary layer to the lower stratosphere, J. Geophys. Res., 111, D16207, 10.1029/2006jd007076, 2006.

Schwarz, J. P., Doherty, S. J., Li, F., Ruggiero, S. T., Tanner, C. E., Perring, A. E., Gao, R. S., and Fahey, D. W.: Assessing Single Particle Soot Photometer and Integrating Sphere/Integrating Sandwich Spectrophotometer measurement techniques for quantifying black carbon concentration in snow, Atmos. Meas. Tech., 5, 2581–2592, 10.5194/amt-5-2581-2012, 2012.

Schwarz, J. P., Perring, A. E., Markovic, M. Z., Gao, R. S., Ohata, S., Langridge, J., Law, D., McLaughlin, R., and Fahey, D. W.: Technique and theoretical approach for quantifying the hygroscopicity of black-carbon-containing aerosol using a single particle soot photometer, J. Aerosol Sci., 81, 110–126, http://dx.doi.org/10.1016/j.jaerosci.2014.11.009, 2015.

Sigl, M., Abram, N. J., Gabrieli, J., Jenk, T. M., Osmont, D., and Schwikowski, M.: 19th century glacier retreat in the Alps preceded the emergence of industrial black carbon deposition on high-alpine glaciers, The Cryosphere, 12, 3311–3331, 10.5194/tc-12-3311-2018, 2018.

Stephens, M., Turner, N., and Sandberg, J.: Particle identification by laser-induced incandescence in a solid-state laser cavity, Appl. Opt., 42, 3726–3736, 10.1364/AO.42.003726, 2003.

Wang, M., Xu, B., Kaspari, S. D., Gleixner, G., Schwab, V. F., Zhao, H., Wang, H., and Yao, P.: Century-long record of black carbon in an ice core from the Eastern Pamirs: Estimated contributions from biomass burning, Atmos. Environ., 115, 79–88, https://doi.org/10.1016/j.atmosenv.2015.05.034, 2015.

~~Wang, D., Guan, D., Zhu, S., Kinnon, M. M., Geng, G., Zhang, Q., Zheng, H., Lei, T., Shao, S., Gong, P., and Davis, S. J.: Economic footprint of California wildfires in 2018, Nat. Sustain., 4, 252–260, 10.1038/s41893-020-00646-7, 2021.~~

Wendl, I. A., Menking, J. A., Färber, R., Gysel, M., Kaspari, S. D., Laborde, M. J. G., and Schwikowski, M.: Optimized method for black carbon analysis in ice and snow using the Single Particle Soot Photometer, Atmos. Meas. Tech., 7, 2667–2681, 10.5194/amt-7-2667-2014, 2014.

Zdanowicz, C. M., Proemse, B. C., Edwards, R., Feiteng, W., Hogan, C. M., Kinnard, C., and Fisher, D.: Historical black carbon deposition in the Canadian High Arctic: a >250-year long ice-core record from Devon Island, Atmos. Chem. Phys., 18, 12345–12361, 10.5194/acp-18-12345-2018, 2018.

Zennaro, P., Kehrwald, N., McConnell, J. R., Schüpbach, S., Maselli, O. J., Marlon, J., Vallelonga, P., Leuenberger, D., Zangrando, R., Spolaor, A., Borrotti, M., Barbaro, E., Gambaro, A., and Barbante, C.: Fire in ice: two millennia of boreal forest fire history from the Greenland NEEM ice core, Clim. Past, 10, 1905–1924, 10.5194/cp-10-1905-2014, 2014.